ORIGINAL RESEARCH ARTICLE

Boride Coatings on Steel Protecting it Against Corrosion by a Liquid Lead-Free Solder Alloy

ZSOLT SALYI, GEORGE KAPTAY, DANIEL KONCZ-HORVATH, LASZLO SOMLYAI-SIPOS, PETER ZOLTAN KOVACS, ATTILA LUKACS, and MARTON BENKE

The goal of this research is to study the applicability of the diffusion boriding process as a high-temperature thermochemical heat treatment to enhance the lifetime of steel selective soldering tools. The main purpose of the work is to discuss the behavior of double-phase (FeB/Fe_2B) iron-boride coating on the surface of different steels (DC04, C45, CK60, and C105U) against the stationary SAC309 lead-free solder liquid alloy. The boride coating was formed on the surface of the steel samples through the powder pack boriding technique. The microstructure of the formed layer was examined by X-ray diffraction (XRD) and scanning electron microscopy (SEM). The borided samples were first cut in half and then immersed into a stationary SAC309 lead-free solder liquid alloy (Sn–3Ag–0.9Cu) for 40 days. Microstructure examinations were performed by SEM with energy-dispersive spectroscopy and an elemental distribution map after the dissolution test. Excessive dissolution/corrosion of the original steel surface was observed at the steel/SAC interfaces, leading also to the formation of Fe–Sn intermetallic phases. This was found to be the major reason for the failure of selective soldering tools made of steel. On the contrary, no dissolution and no intermetallic compounds were observed at the FeB/SAC and at the Fe_2B/SAC interfaces; as a result, the thicknesses of the FeB and Fe_2B phases remained the same during the 40-day dissolution tests. Thus, it was concluded that both FeB and Fe_2B phases show excellent resistance against the aggressive liquid solder alloy. The results of the dissolution tests show a good agreement with the thermodynamic calculations.

https://doi.org/10.1007/s11663-021-02412-2

I. INTRODUCTION

THE degradation of selective soldering tools has increased significantly with the application of lead-free solders. Although these solders comply with the European Union directives—no lead content—the new tin-based solders damage the iron base material of the tool and an intermetallic compound phase is formed in this surface, which continuously thickens with the soldering time.[1–4] Formation of the intermetallic compound phases, FeSn and $FeSn_2$, between iron and tin takes place according to the iron-tin equilibrium phase diagram at the soldering temperature (about 573 K).[5] This was confirmed by several studies;[6–8] however, other molten metals (*e.g.*, Al) also form intermetallic compound phases with iron.[9–12] Due to the different thermal expansion of the formed compound phase, it peels from the tool surface and interrupts the continuity of the solder wave.[13] However, the destabilization of the solder wave will result in the replacement or renewal of the tool, which causes significant cost and downtime. During the renewal of the soldering tools, the intermetallic $FeSn_2$ layer is removed from the surface of the tool and then a nickel coating is formed, which is also well wetted by the lead-free solder. However, nickel also forms an intermetallic compound with the tin and tool failure occurs.[4,14] Therefore, this solution is not a complete or long-term one for extending the life of selective soldering tools. Because soldering companies

ZSOLT SALYI, LASZLO SOMLYAI-SIPOS, and MARTON BENKE are with the Institute of Physical Metallurgy, Metalforming and Nanotechnology, University of Miskolc, Miskolc-Egyetemváros 3515, Hungary. Contact email: femsalyi@uni-miskolc.hu GEORGE KAPTAY is with the Institute of Physical Metallurgy, Metalforming and Nanotechnology, University of Miskolc, and also with the MTA-ME Materials Science Research Group, ELKH, Miskolc-Egyetemváros 3515, Hungary. DANIEL KONCZ-HORVATH is with the Advanced Materials and Intelligent Technologies Higher Education and Industrial Cooperation Centre (HEICC), Miskolc-Egyetemváros 3515, Hungary. PETER ZOLTAN KOVACS is with the Institute of Material Science and Technology, University of Miskolc, Miskolc-Egyetemváros 3515, Hungary. ATTILA LUKACS is with Flextronics International LTD, Zalaegerszeg 8900, Hungary.

Manuscript submitted August 17, 2021; accepted November 30, 2021.
Article published online January 12, 2022.

are secretive regarding handling of these problems within the industry, there is hardly any literature in this field of science.

There are few methods in the literature that would prevent or reduce the formation of the intermetallic compound phase. One possible method is the modification of the solder alloy. Nishikawa *et al.* reduced the formation of the $FeSn_2$ compound phase by adding some Co to the solder. Although the process is really functional, the quality and reliability of the solder joints are changed adversely.[15] Watanabe *et al.* investigated the resistance of Fe-MWCNT (multiwall carbon nanotube) composite in lead-free solder melt. Their research showed that the resistance of the composite material increases, whereas the wetting of the surface by liquid SAC decreases, which is also an important parameter for the stability of the solder wave.[16] In addition, the production of the composite is much more expensive, and the cost-effective production of the tool is also an important aspect. Thus, the lifetime of the tool cannot be improved, or only to a negligible extent, by modifying the solder alloy with composite materials.

Protecting and modifying the surface of the soldering tool is a much more viable method.[17,18] The use of thermochemical heat treatments to protect soldering tools is a possible new, but less investigated, solution. Among other things, boriding is one such treatment where the surface of a steel substrate is enriched with boron, thus forming iron borides (FeB, Fe_2B) on the surface.[19–23] The high hardness and abrasion resistance of the boride layer are preferred by the soldering industry, where the detrimental consequences of friction and deformation are indicated due to high loads.[24–30] In addition to its excellent mechanical properties, the resistance of the boride layer against various molten metals and corrosive media (acids, alkalis) is also significant. The literature shows in detail the significant resistance of the boride layer against Zn melt, where even a tenfold increase in the life of the component can be achieved by boriding. This is confirmed by several studies.[31–35] The boride layer is similarly resistant to Al melts. After dissolution tests, no reaction product was detected between the boride layer and the aluminum.[35–37] The resistance of the boride layer to acids and alkalis is also significant. The layer is resistant to sulfuric acid, phosphoric acid, sodium hydroxide, and perchloric acid; however, hydrochloric acid and nitric acid corroded the borided surface.[38–40] The wettability of the iron-boride layer with solder melts has not been investigated in the literature yet, nor has the use of boriding to extend the lifetime of selective soldering tools. Thus, this research represents a new application of the boride layer. In some reports, the wetting properties of the boride layer (especially the Fe_2B phase) were investigated against Zn melt but poor wettability was found.[41,42] Passerone *et al.* found that pure molten metals generally do not wet ceramic materials.[43] On the other hand, nitrides, carbides, and borides of transition metals are metal-like compounds that are usually well wetted by liquid metals, provided the oxide layer is excluded by a molten salt/flux layer.[44,45]

The literature of borided steels does not discuss the metallurgical interaction between the borided layer and the lead-free solders and does not investigate the resistance of the iron-boride layer against SAC-based lead-free solder melts. Furthermore, the literature does not detail the corrosion resistance of either FeB or Fe_2B against liquid lead-free solder alloys and does not describe the metallurgical processes at the interface. The goal of this article is to study the corrosion resistance of the double-phase iron boride layer against a stationary SAC309 lead-free liquid solder alloy.

II. MATERIALS AND METHODS

A. *Materials*

For the immersion test, rectangular shape DC04, C45, CK60, and C105U steels were used with 17 mm × 12 mm × 5 mm size (DC04: 17 mm × 12 mm × 1 mm) and the same shape but only 10 mm × 7 mm × 3 mm (DC04: 10 mm × 7 mm × 1 mm) size specimens were used for the contact angle measurement. Table I summarizes the chemical composition of the chosen steels. For the dissolution tests, SAC309 lead-free solder alloy was used (Table II provides its chemical composition).

B. *Diffusion Boriding*

After cutting and machining, the samples were cleaned and degreased with petrol-based stain remover. Then, solid medium boriding (powder boriding) was carried out on the steel substrates. The specimens were

Table I. Chemical Composition of the Examined Steels, Nominal (Weight Percent)

Material	Number	C	Mn	Si	Ni	Cr	Mo	P	S
DC04[46]	1.0338	max 0.08	max 0.4	—	—	—	—	max 0.03	max 0.03
C45[47]	1.0503	0.43 to 0.5	0.5 to 0.8	max 0.4	max 0.4	max 0.4	max 0.1	max 0.045	max 0.045
CK60[48]	1.1221	0.57 to 0.65	0.6 to 0.9	max 0.4	max 0.4	max 0.4	max 0.1	max 0.03	max 0.035
C105U[49]	1.1545	1 to 1.1	0.1 to 0.4	0.1 to 0.3	—	—	—	max 0.03	max 0.03

Table II. Chemical Composition of the SAC309 Solder Alloy Determined by ICP (Weight Percent)[50]

Sn	Ag	Cu	Ni	Fe	Bi	Pb	Sb
Bal	2.85	0.96	0.0072	0.108	0.0048	0.0245	0.0106

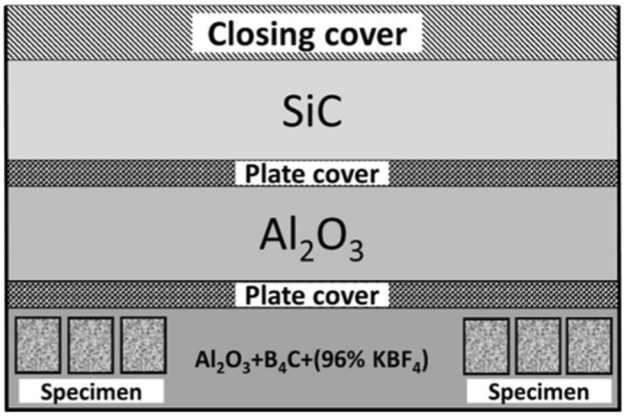

Fig. 1—Schematic of the boriding container.

inlayed in a steel container and then embedded in a special powder mixture: 5 wt pct B_4C as boron source, 5 wt pct KBF_4 as activator, and 90 wt pct Al_2O_3 as diluent. The masses of the components of the applied powder mixture during the process are 15 g B_4C, 15 g KBF_4, and 270 g Al_2O_3. The total surface area of all samples was 26,400 mm^2. After a compression process, the mixture with the steel specimens was closed down with a plate cover. To avoid oxidation, thick layers of aluminum oxide and silicon carbide powder were applied on the top of the plate cover and were also compressed. The top of the boriding container was finally closed with a steel cover. Figure 1 illustrates the structure of the steel boriding container. The closed container was inserted in a three-phase resistance-heated chamber furnace at 1183 K (910 °C) for 3.5 hours. After thermochemical heat treatment, the samples were removed and cleaned for further tests and microstructural analysis.

C. *Microstructure Analysis*

Phase analysis was carried out with a Bruker D8 Advance type X-ray diffractometer using a Co K_α X-ray source. The microstructure analysis was performed with a Zeiss EVO MA 10 scanning electron microscope equipped with an energy-dispersive spectrometer (energy-dispersive X-ray analysis EDS) and a Helios G4 PFIB CXe (Thermo Fisher Scientific (Waltham, MA)) plasma focused ion beam scanning electron microscope.

D. *Immersion Test*

Before the examination of dissolution behavior, the borided samples were cut in half to let the SAC309 get in direct contact with both the FeB and Fe_2B phases. Thus, all three interfaces (FeB/SAC309, Fe_2B/SAC309, and steel/SAC309) were studied in a single experiment for a given steel sample. Immersion tests were performed in a self-built dissolution test simulator in which the samples were submerged into SAC309 solder melt for 40 days. Detailed information about the dissolution test simulator can be found in References 17 and 18. The test temperature was set to 593 K (320 °C).

E. *Contact Angle Measurement*

The sessile drop method was used for the wetting experiments. For the measurements, 10 mm × 7 mm × 3 mm rectangular borided specimens were used (DC04: 10 mm × 7 mm × 1 mm). Note that the exact weight of the applied solder shavings during the contact angle measurement is an important consideration due to the comparability of unified parameters. The mass of 0.0043 to 0.0049 g SAC309 solder shavings was prepared and cleaned together with the borided substrates in 10 wt pct sodium hydroxide. Alkaline purification was followed by a wash with distilled water and a rinse with ethanol. Finally, the samples were air dried. In order to reproduce the industrial soldering conditions as closely as possible, the wettability tests were performed in air atmosphere. However, to remove the surface oxide layer, a flux-type INOfuX (= mixture of < 100 wt pct zinc-chloride, < 20 wt pct sodium-phosphate-dodecahydrate, < 20 wt pct iron(III)-chloride hexahydrate, < 10 wt pct ammonium chloride, and < 2 wt pct sodium fluoride)[51] was applied, the same way as it is done in the industry. The flux was added to the surface of the borided samples; then the solder shavings were placed in the center of the borided steel substrate.[52] The compiled system was inserted in a preheated horizontal vacuum tube furnace (Sunplant Ltd., Miskolc) equipped with a CCD camera. After the installation of the samples, the furnace was heated to 593 K (320 °C) and an isothermal annealing was applied in within ± 10 °C for 180 seconds without use of vacuum. After the annealing process, the samples were cooled to room temperature spontaneously inside the furnace. The contact angle of the lead-free solder droplet was measured with the use of KSV software following the Young–Laplace method.[53] The contact angle values measured on the right and left sides of the solidified solder droplet silhouette were averaged. The tolerance in the case of wetting investigations was within ± 3 deg. The tests were repeated 5 times in parallel on all borided steel samples, and in order to investigate the effect of oxidation for the wetting properties of the boride layer, one sample of each borided steel material was oxidized at 300 °C for 2 hours under air atmosphere. The method to measure the contact angle values on the specimens was then carried out according to the same previously described procedure.

III. RESULTS

A. *Microstructure of the Borided Samples Prior to Immersion Tests*

The microstructures and layer thickness values of the borided steels are shown in Figure 2. It can be seen that for all examined steels, the boride layer consisted of a compact region (with a thickness of ~ 30 μm) and, beneath, the "sawtooth" morphology of the borided layer was found. The thickness of the compact section depends on the alloying elements of the steels.

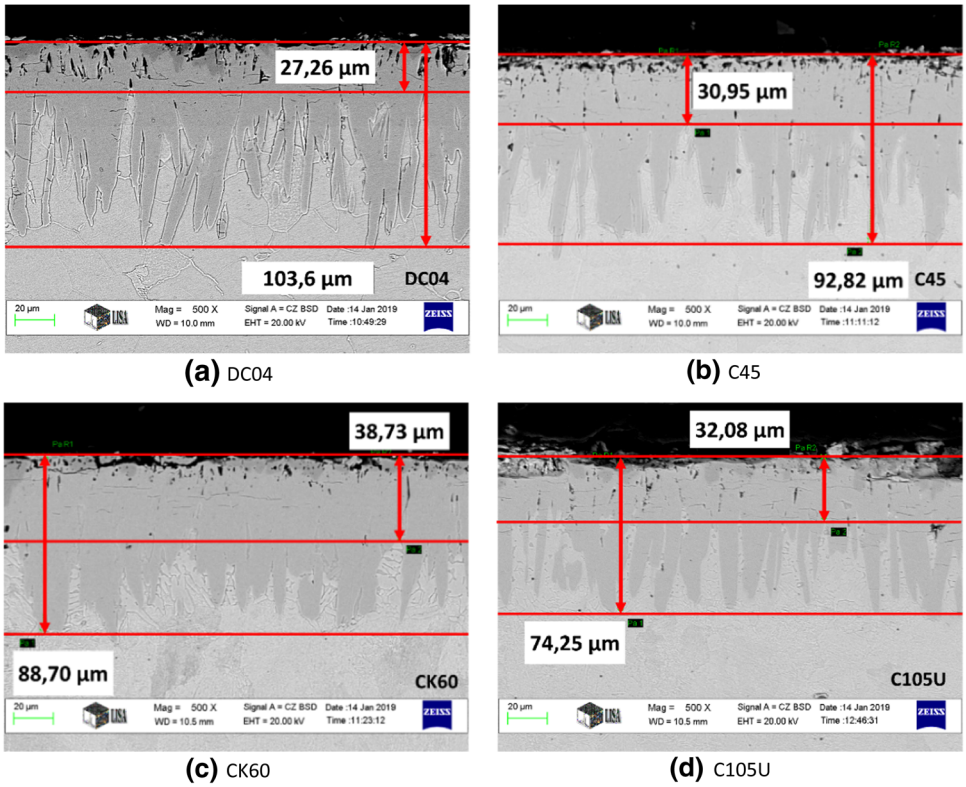

Fig. 2—SEM image of the borided region of the examined steels.

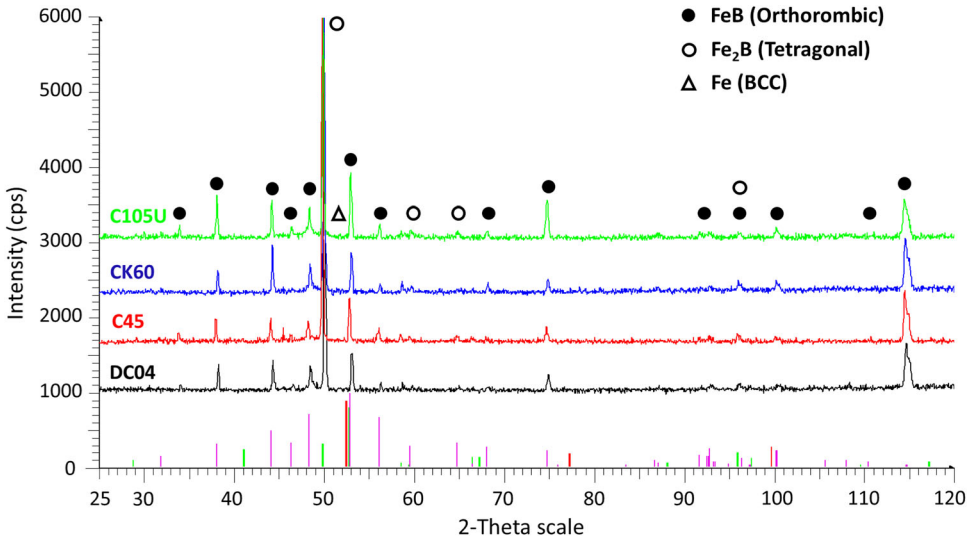

Fig. 3—XRD spectra and formed phases of the borided steel samples.

The phases formed near the surface of the borided steels were identified by X-ray diffraction (XRD) phase analysis. The XRD spectra of the borided steels are shown in Figure 3.

As shown in Figure 3, XRD phase analysis revealed that Fe_2B phases with tetragonal crystal structure and orthorhombic FeB phases were formed on surfaces of all the borided steels. Other phases were not detected. It is worth mentioning that for all detected borides, the relative intensities strongly differ from the isotropic case, suggesting that the formed phases are textured.

B. *Microstructure of the Borided Samples after Immersion Tests*

Figures 4 through 7 show the microstructures of the samples after immersion tests. On the element maps, green corresponds to Ag, indicating the presence of Ag_3Sn phases, and orange corresponds to Cu, marking the presence of Cu_6Sn_5 phases within the liquid solder alloy (or after it was cooled). The element map of Ag and Cu is not presented since it was not relevant in this investigation. The element map of B was not relevant as well, because the maps were prepared by EDS analysis, which is not a suitable technique for exact boron detection. In the case of boron, the difference between the energies of the electron orbits is extremely small; thus, the X-ray photon that can be detected has very little energy (0.17 keV). In addition, due to low energy, the loss of X-ray photons is also significant. According to the images, no reaction product phases formed at the FeB/SAC309 and Fe_2B/SAC309 interfaces of the examined samples. The element maps of Sn and Fe also prove that there is no dissolution or reaction between the boride and the liquid SAC phases. It is also apparent that the morphology and thickness of the FeB and Fe_2B phases did not change during the immersion tests. On the other hand, the dissolution of Fe atoms and the formation of the $FeSn_2$ intermetallic compound phase were detected at the steel/SAC309 interfaces for all steel samples studied. The highest extent of dissolution occurs in the case of DCO4 steel, which has the lowest alloying elements and carbon content. By increasing the carbon content and the concentration of some alloying elements, the dissolution of Fe atoms is decreased, but without a boride layer, the degradation process between the steel and lead-free solders is unavoidable. It can be seen that some Fe_2B crystals are surrounded by the ex-liquid solder, which dissolved some part of the steel matrix around the Fe_2B crystals, but no reaction phases are present at the Fe_2B interfaces, proving in the most obvious way the corrosion rate difference between the steel matrix and the iron borides (Figure 4). It can also be observed in Figures 4 through 7 that the formed $FeSn_2$ phase partly surrounds the Fe_2B phase, which maintains its original morphology. Thus, it can be concluded that both FeB and Fe_2B phases of the boride layer are resistant against corrosion by the SAC309 solder melt.

C. *Results of the Wettability Tests*

Table III represents the measured contact angle values between the FeB phase and the SAC309 solder melt.

The contact angle measurements indicated a good wettability of the boride layer on all steel substrates with the SAC309 melt. With the applied parameters, the SAC309 lead-free solder melt wets well the surface of borided steels. This is in agreement with some previous literature and proves that iron borides are metal-like refractory compounds, which behave similarly to TiC or TiB_2 phases in terms of their wettability by liquid metals.[44,45]

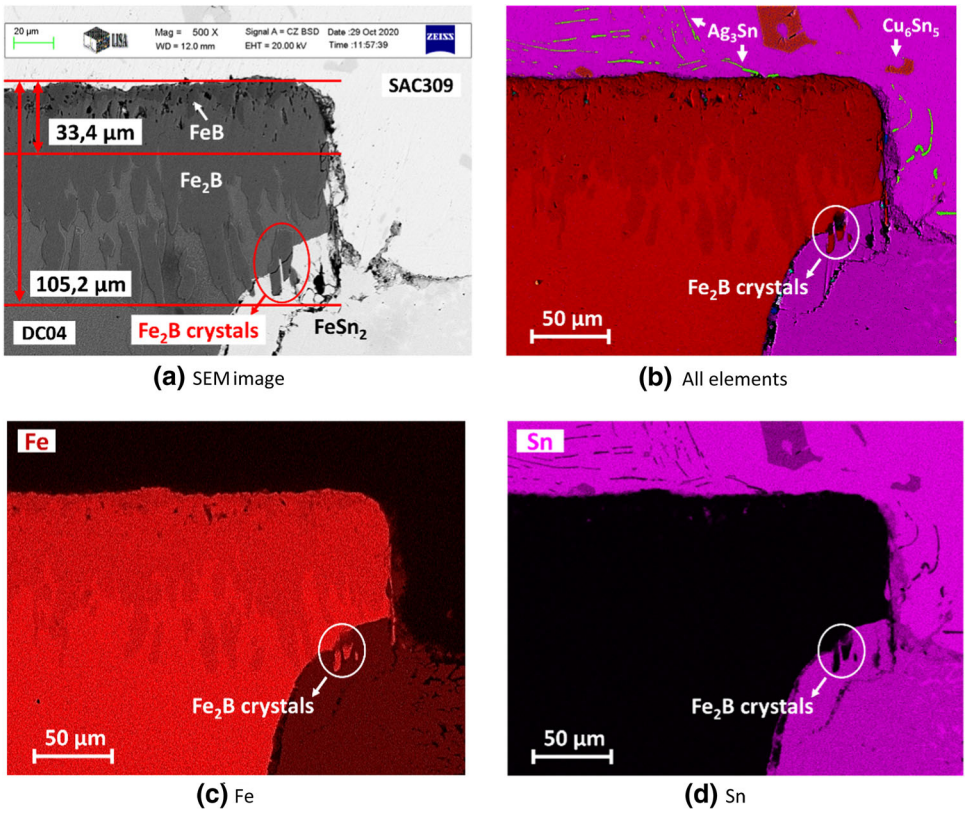

Fig. 4—Elemental distribution map of the borided DC04 after the dissolution test.

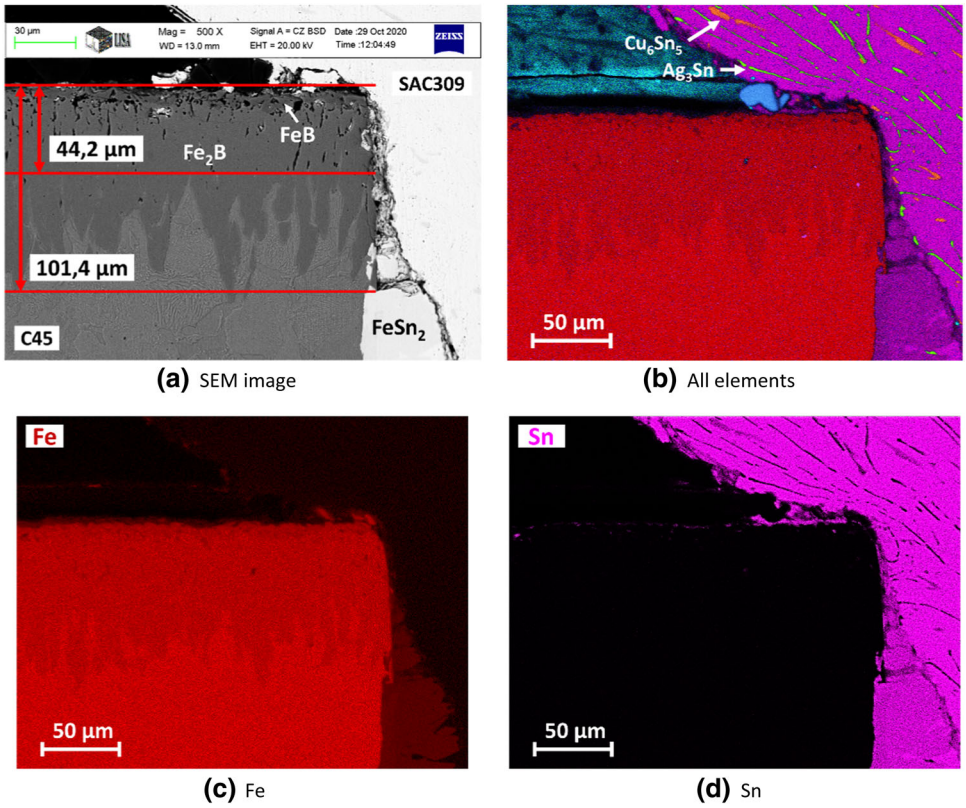

Fig. 5—Elemental distribution map of the borided C45 after the dissolution test.

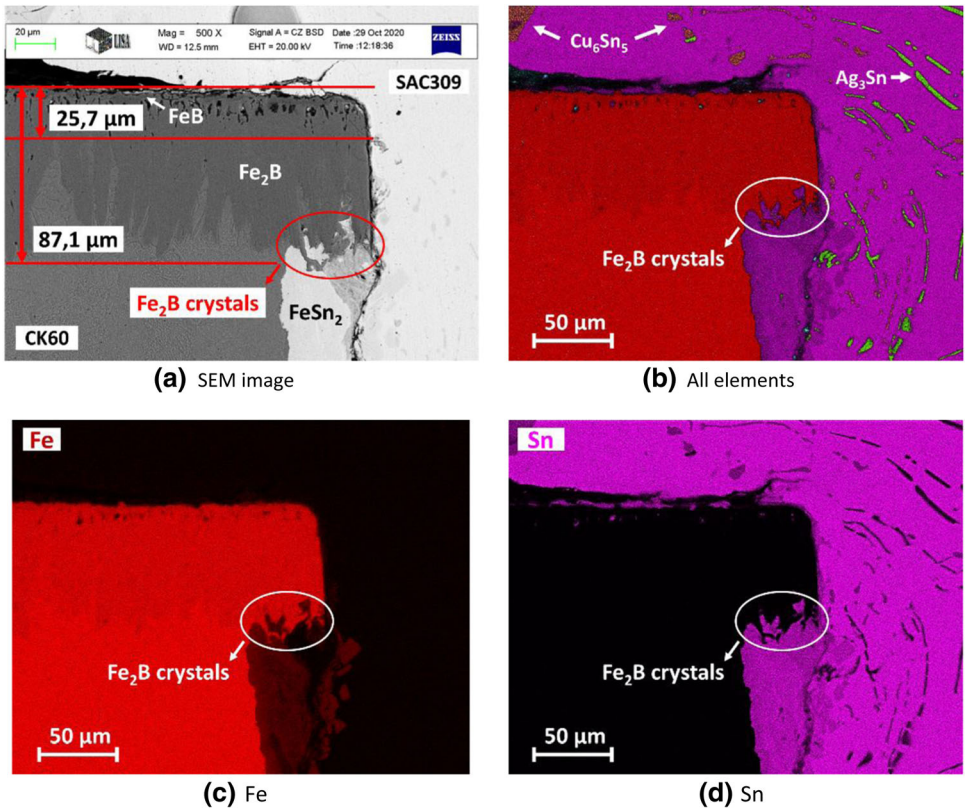

Fig. 6—Elemental distribution map of the borided CK60 after the dissolution test.

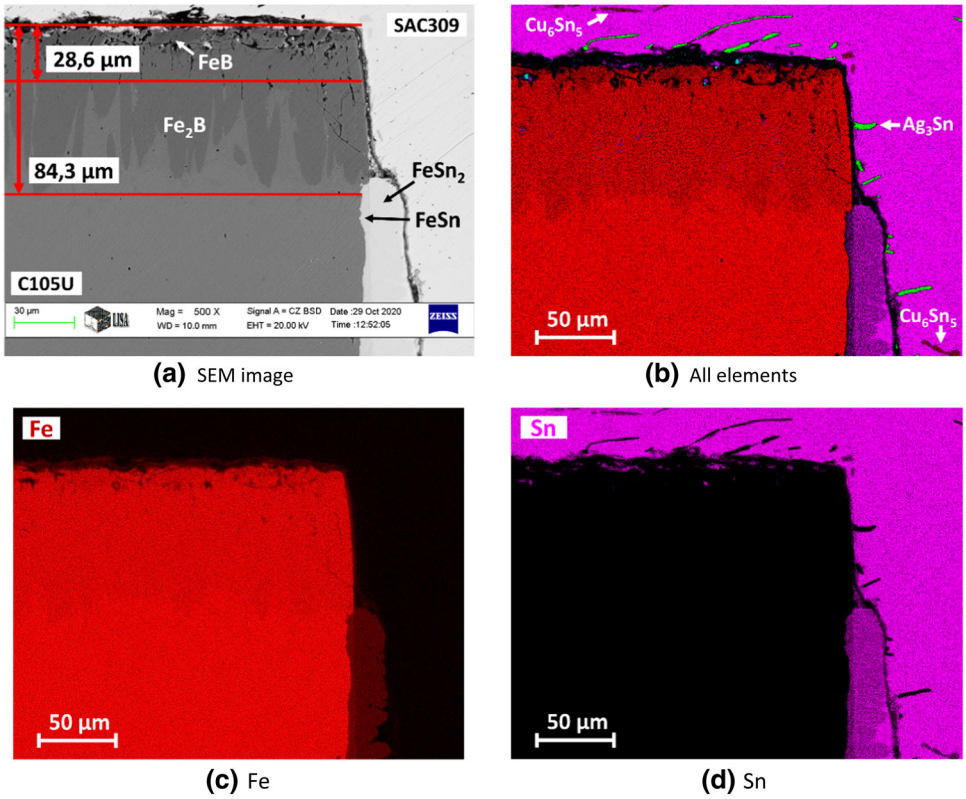

Fig. 7—Elemental distribution map of the borided C105U after the dissolution test.

Table III. Contact Angle Values in the FeB/SAC309 Interface (±3 Deg)

Borided Steel	Weight of the Solder Shavings (g)	Four Measured Contact Angles on Nonoxidized Samples (Deg)	Measured After Oxidizing the Sample (Deg)
DC04	0.0043	20/11/34/33	20
C45	0.0045	23/11/17/57	11
CK60	0.0045	31/41/19/14	30
C105U	0.0049	29/60/11/12	34

Table IV. Standard Molar Gibbs Energies of Formation of Some Compounds From Their Elements at Two Temperatures[54,55]

T (K)	B_4C[54]	FeB[54]	Fe_2B[54]	Fe_3C[54]	$FeSn_2$[55]	FeSn[55]
593	—	–68.9	–69.7/–75.8*	—	–36.6	–30.5
1183	–74.4	–66.7	–65.5/–73.4*	–12.9	—	—

*Corrected values in this article (refer to the text for details).

IV. DISCUSSION

In this section, the thermodynamic possibilities of different chemical interactions will be analyzed to provide a more solid theoretical basis for our experimental results. In Table IV, the standard molar Gibbs energies of formation of some compounds are shown from their elements at two temperatures of interest in this article.[54,55]

According to the Fe-B phase diagram,[56] at 912 °C, the alpha-gamma phase transition takes place in pure iron and in two-phase iron/Fe_2B mixtures. As the solubility of B in pure solid iron is negligible, the transition temperature of 912 °C is not a function of the average boron content of the alloy. Below 1389 °C, two stable borides exist in the phase diagram: the Fe-rich Fe_2B and the equimolar FeB compounds. Both are close to perfectly stoichiometric compounds, with negligible solubilities of Fe and B. The lowest melting point liquid phase in the system is the eutectic between pure gamma-Fe and Fe_2B phases at 1174 °C. The equimolar FeB compound melts incongruently at 1650 °C.[56]

Unfortunately, some standard molar Gibbs energy values taken from Reference 54 contradict the phase diagram.[56] The latter is preferred by us as a more reliable source. According to the phase diagram, the

chemical reaction FeB + Fe = Fe_2B should be accompanied with a negative standard molar Gibbs energy change at least below the eutectic temperature of 1174 °C. However, applying data from Table III (remembering that the standard molar Gibbs energy of pure iron is zero by definition), the molar Gibbs energy change accompanying this reaction is – 0.8 kJ/mol-FeB at 593 K (320 °C) (which might be correct) and is + 1.2 kJ/mol at 1183 K (910 °C) (which is surely wrong). From the requirements dictated by the Fe-B phase diagram, the standard molar Gibbs energy of formation of the Fe_2B phase from the elements should be between 1 and 2 times the standard molar Gibbs energy of the FeB phase from the same elements at any temperature below the eutectic temperature of 1174 °C. As according to Barin[54] the standard molar Gibbs energy values for the two compounds are close to each other (Table IV), the standard molar Gibbs energy values for the Fe_2B phase are selected in the first approximation as 1.1 times the same for the FeB compound (corrected data marked with an asterisk in Table IV). These corrected data will be applied further in this article.

A. *On the Processes Taking Place during Boriding the Steels*

Boriding was performed by using the powder mixture of (B_4C + Al_2O_3 + KBF_4) in contact with the steel samples at 910 °C. The rate limiting factor of boriding is diffusion; so, the higher the temperature, the faster the process. However, the temperature should not be above that of the alpha-gamma phase transition of iron (912 °C) to avoid cracking of the coating upon cooling due to phase transition of the steel. This is how the optimum (maximum possible) temperature of 910 °C was selected.

The KBF_4 powder melts at 570 °C and perfectly wets all phases, including the B_4C particles and the steel surface. But, as the KBF_4 phase is thermodynamically too stable to participate in the boriding process, the function of the KBF_4 phase is only to provide a medium to dissolve and to transfer by diffusion the boron ions from the B_4C particles to the steel surface. Additionally, KBF_4 dissolves the oxide layer from the steel parts. The following chemical reaction takes place when the first boron ions contact the KBF_4/steel interface (written as a summary chemical reaction): $B_4C + 8Fe = 4Fe_2B + C$, accompanied with – 219.2 kJ of standard Gibbs energy change (Table III). After the thickness of Fe_2B reaches the magnitude of about 100 nm, the flux of B ions becomes faster through the liquid KBF_4 phase compared to the flux of B atoms through the solid Fe_2B phase. As a result, some excess of B ions will be accumulated at the KBF_4/steel interface. Therefore, the following second chemical reaction will take place: $Fe_2B + B = 2FeB$, accompanied with – 60.0 kJ of standard Gibbs energy change (Table III). As the boron atoms are much smaller (0.083 nm in radius[57]) than Fe atoms (0.1241 nm in radius[57]), both boride phases will grow mostly by the diffusion of B atoms through them, while the role of the flux of Fe atoms through the same boride phases will be negligible. This will take place until the high activity of B remains at the KBF_4/steel interface.

From the 15 g of B_4C, the maximum of 72.1 g of FeB or maximum of 132.6 g of Fe_2B can form. Dividing these values by the density of 6.62 g/cm^3 of FeB[58] and by the density of 6.81 g/cm^3 of Fe_2B,[59] the maximum possible volume of 10.9 cm^3 of FeB or the maximum possible volume of 19.5 cm^3 of Fe_2B is obtained. Dividing these values by the total surface area of the treated steel samples (264 cm^2), the maximum possible thickness of 413 μm of FeB or the maximum possible thickness of 737 μm of Fe_2B is obtained. Comparing these maximum possible theoretical thickness values with the experimental results shown in Figure 2, one can see that only about 10 to 20 pct of the maximum boriding capacity was actually used by us.

Let us note further that the formation of iron carbide is expected to take place as a result of the reaction $B_4C + 11Fe = Fe_2B + Fe_3C$ as it is accompanied by – 232.1 kJ of standard Gibbs energy change, being more negative compared to the – 219.4 kJ accompanying the first process explained previously: $B_4C + 8Fe = 4Fe_2B + C$. Iron carbide, however, does not form for kinetic limitations: Carbon atoms/ions have negligible solubility in liquid KBF_4 and, thus, the flux of carbon atoms/ions through the liquid KBF_4 flux is negligible compared to the flux of boron ions through the same phase. Therefore, graphite particles will precipitate at the B_4C/KBF_4 interface during boriding the steel (Figure 8). It should also be remembered that boron diffusion into steel along its grain boundaries is much faster compared to the diffusion of boron through the steel grains, leading to the sawtooth morphology of the steel/Fe_2B interface (compare Figures 8 and 2).

Now let us consider the case when the boron activity is dropped in the surroundings of the steel sample already coated, as shown in Figure 9. This might take place due to the removal of the steel samples from the (KBF_4 + B_4C) mixture or due to the full consumption of B_4C particles. Then, the following process will take place: Fe + FeB = Fe_2B, accompanied with – 6.7 kJ of standard Gibbs energy change. The rate of this latter process is also limited by the boron diffusion through the Fe_2B layer. As a result, if boriding is performed in high-boron-activity medium, the resulting structure will be Fe/Fe_2B/FeB (Figure 8). Although this (or a similar) structure can remain for a long time, even in the absence of a high-boron-activity environment, this is not the equilibrium structure, at least if the amount of Fe is much larger in the system compared to the amount of B (which is the practical situation if steel is borided and boron is not ironed).

Upon heat treatment performed in a low-boron-activity medium, the outer FeB coating will gradually disappear and the resulting structure will be Fe/Fe_2B (Figure 9). Moreover, let us note that the sawtooth microstructure formed due to the high diffusion rate of boron along grain boundaries in high-boron-activity environment is not an equilibrium structure in a low-boron-activity environment, due to its high specific interface.[60] Therefore, with time of heat treatment, it is expected that the specific interface area of the Fe_2B phase will gradually decrease, as shown in Figure 9.

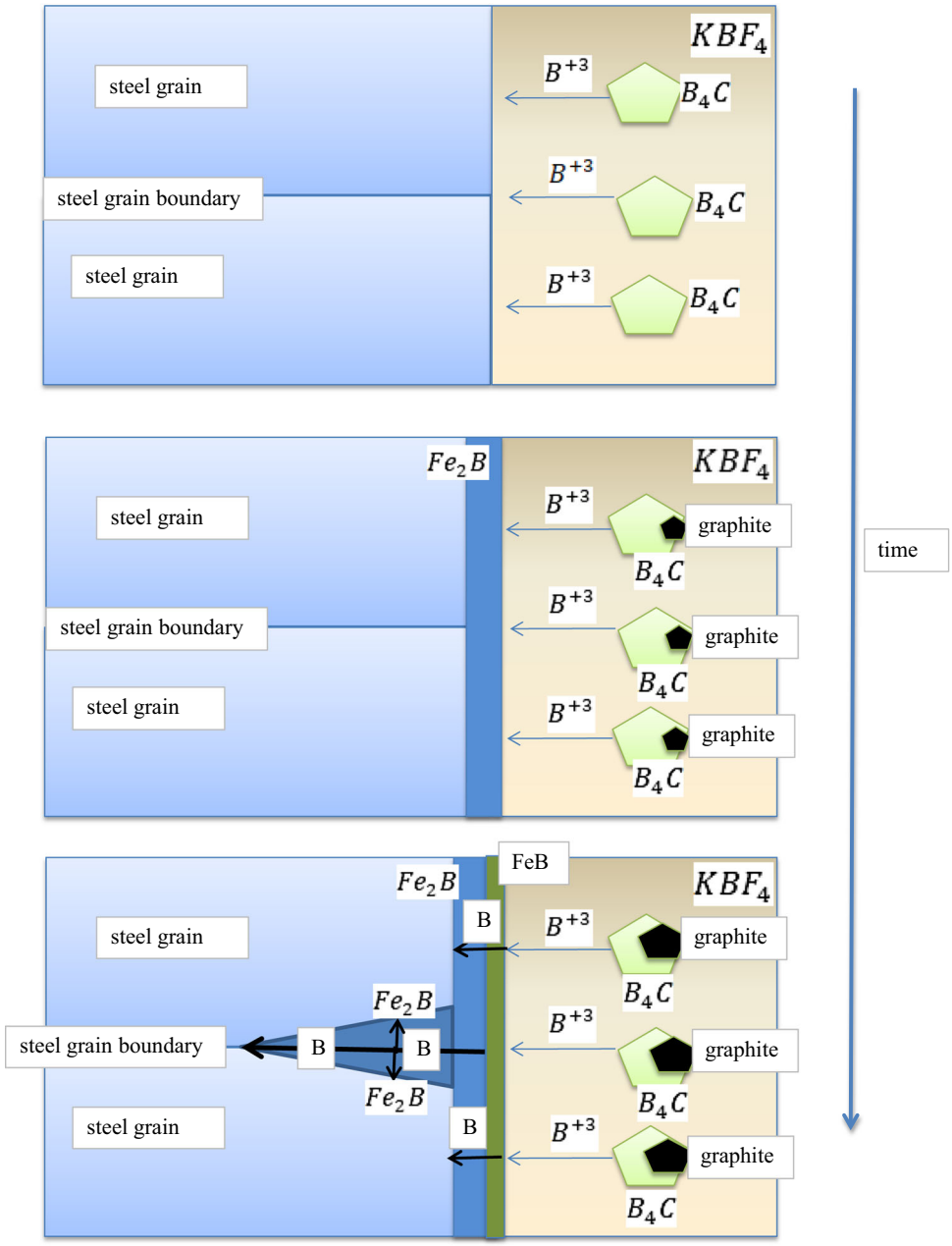

Fig. 8—Schematic of the processes taking place during boriding steels by the mixture of B_4C + KBF4 (in a high-B-activity medium). Thin arrows show the diffusion flux of B^{+3} ions through liquid KBF_4, while thick arrows show the diffusion flux of B atoms through the FeB and Fe_2B phases.

As follows from Figures 8 and 9, both FeB and Fe_2B can be in contact with liquid solder alloys. This means that both the FeB and Fe_2B phases should be tested for their corrosion resistivity in liquid soldering alloys to make sure that the boride coating provides sufficient protection to steel.

As follows from Table I, our investigated steels contain some C, Mn, and Si in addition to the majority of Fe atoms. A B_4C phase in steel will surely not form, as the process to transfer B atoms from pure B_4C particles of the (B_4C + KBF_4) powder mixture toward the dissolved carbon atoms in steel is accompanied by a positive molar Gibbs energy change. The Mn-boride and Si-boride phases could form if pure Mn or pure Si phases were present in the (B_4C + KBF_4) mixture, but according to the corresponding phase diagrams and thermodynamic properties, such borides will not be formed in steels with low Si and low Mn content, as shown in Table I. Thus, only Fe_2B and FeB phases are expected to form during boriding of steels of Table I, in agreement with experimental observations.

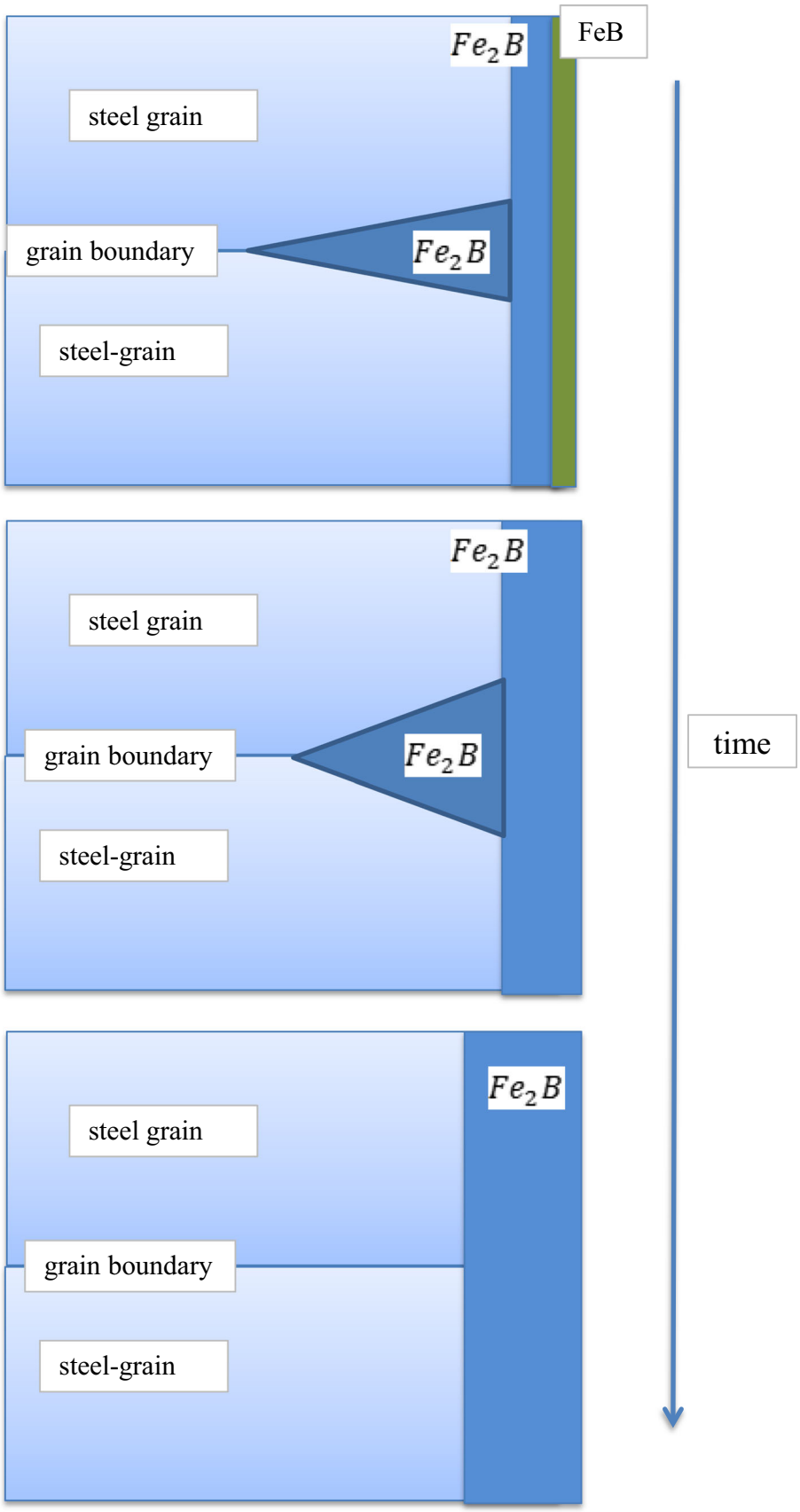

Fig. 9—A gradual transformation of the initial steel/Fe_2B/FeB microstructure into a more and more stable steel/Fe_2B microstructure as a function of time in low-B-activity medium.

Table V. Standard Gibbs Energy Changes Accompanying Some Chemical Reaction at 593 K (320 °C) (kJ/mol, Data From Table IV)

Reactions	$\Delta_r G°$(kJ/mol)
$FeB + Sn = FeSn + B$	+38.4
$FeB + 2Sn = FeSn_2 + B$	+32.3
$Fe_2B + 2Sn = 2\ FeSn + B$	+14.8
$Fe_2B + 4Sn = 2\ FeSn_2 + B$	+ 2.6
$Fe + Sn = FeSn$	–30.5
$Fe + 2Sn = FeSn_2$	–36.6

B. *On the Corrosion of Steels in Liquid Solder Alloys*

Liquid lead-free solder alloys contain tin as a majority element with some silver and copper as alloying elements. Liquid tin is known to dissolve iron and to form intermetallic compounds with it, but Cu and Ag are known to be inert in contact with iron, especially at a low temperature of 320 °C.[56] Therefore, the corrosive effect of SAC309 will be modeled here in the first approximation as the corrosive effect of liquid tin.

As follows from Table IV, the formation of both FeSn and $FeSn_2$ intermetallic compounds is accompanied by a negative standard Gibbs energy change (also the last lines of Table V). Therefore, it is not surprising that during the 40-day tests, the uncoated parts of our steel samples were partly dissolved in stagnant liquid tin or intermetallic compounds were formed at the original steel/SAC interface (Figures 4 through 7).

C. *On the Corrosion of Iron Borides in Liquid Tin*

None of the three components of the SAC309 liquid solder alloy forms any boride or dissolves boron at temperatures around 320 °C.[56] Therefore, to theoretically check the corrosive action of liquid SAC alloys on iron borides, their possible chemical reactions are considered with liquid tin, leading to the formation of Fe–Sn intermetallics and a boron phase. As follows from Table V, all chemical reactions between iron borides and liquid tin at 320 °C are accompanied by a positive standard Gibbs energy change. This explains why both iron borides remained intact during our 40-day immersion tests in liquid SAC309. Since the reactions between FeB and Sn are accompanied by more positive standard Gibbs energy changes compared to the reactions between Fe_2B and Sn (Table V), the FeB phase is more stable in terms of long-term protection in liquid tin compared to the Fe_2B phase.

D. *Influence of Oxidation on Wettability of Borided Steel by Liquid Tin*

Some borided steel was oxidized in normal air atmosphere during 2 hours at 300 °C. It was found that the contact angle of liquid Sn measured on these samples decreased from the range of 11 to 60 deg for nonoxidized samples to the range of 11 to 34 deg for oxidized samples (Table III). In this section, the reasons behind this observation are revealed.

Let us clarify that the low-temperature heat treatment was not sufficient to lose the B atoms of the FeB and Fe_2B phases due to the low volatility of the B atoms. The first hypothesis is that the boride layers are fully oxidized, and during contact angle measurement, they are removed by the flux; so, in this case, the contact angle of Sn is measured on bare steel. To prove or disprove this hypothesis, the thickness of oxidized boride layer is estimated using the experimental results reported in the literature.[61,62] Ptačinová *et al.*[62] measured the oxidation kinetics of similarly boridized steel samples at 873 to 1173 K and found a parabolic mass increase. From this, they provided a kinetic constant at the lowest measured temperature of 873 K (1.039×10^{-9} kg^2/m^4s) and their activation energy of 93 kJ/mol of the low-temperature part of their results; the kinetic constant at our 300 °C = 573 K is estimated as 1.28×10^{-12} kg^2/m^4 s. Multiplying this constant by our oxidation time of 2 hours and taking the square root of the result, 9.58×10^{-5} kg/m^2 is found as a surface area specific mass increase of the sample. This mass increase is due to the chemical reaction $FeB + 1.5\ O_2 = FeBO_3$, which leads to the 72 pct mass increase compared to the initial mass of the sample. Thus, the original surface area specific mass of the to be oxidized FeB was $9.58 \times 10^{-5}/0.72 = 1.33 \times 10^{-4}$ kg/m^2. Dividing this value by the density of FeB (6620 kg/m^3[58]), the oxidized thickness of FeB is found as 1.9×10^{-8} m = 19 nm. This thickness is lower more than 100 times compared to the thickness of the originally deposited outer FeB layer, meaning that the majority of the initial iron boride coating remained on the steel surface unoxidized. Similar results can be found from the independent measurements of Suwattananont *et al.*,[61] who measured the parabolic rate constant at the lowest temperature of 773 K to be 1.05×10^{-10} kg^2/m^4 s with the activation energy of 96 kJ/mol. Extrapolating these data to our temperature of 573 K, the estimated rate constant is 1.14×10^{-12}. Repeating the same procedure as described previously, the oxidized FeB thickness is found as 18 nm, practically the same as found earlier. This proves that our first hypothesis was wrong and our oxidizing treatment could not oxidize the boride layer. "However, it should be noted that the stability of the iron-boride layer is reduced applying higher temperature or oxidizing environment, leading to a more significant oxidation."[63,64]

Our second hypothesis is that the oxidative treatment could clean the boride surface from contaminants. The surface contamination after our boridizing might be the mixture of particles of Al_2O_3, B_4C, and graphite (the latter being the dissociation product of B_4C during the process in which the B content of B_4C was consumed to boridize steel and graphite particles were left over). Oxidation of this mixture of particles leads to the same Al_2O_3 (unchanged), B_2O_3, and volatile CO_2. The two solid oxides are removed by the flux during the contact angle measurement. Thus, we found that our oxidative

treatment cleaned the original boridized surface from graphite and B_4C particles, which are not solvable in the flux.

As shown in References 65 through 67, the contact angle of liquid tin on graphite is between 129 and 135 deg and it only weakly depends on temperature. Similar values are expected for B_4C, as both graphite and B_4C are covalently bonded phases and so they are able to create only a weak van der Waals type adhesion energy with liquid metals.[66] This is further confirmed by experiments.[68–70]

As a result, we can conclude that the wettability of the cleaned (partly by oxidation and partly by the flux) FeB surface has a somewhat better wettability by liquid tin compared to the uncleaned surface. Also, the measured wettability of liquid tin on the uncleaned surface has a large scatter of contact angle by liquid tin, due to uncontrolled amounts of poorly wetted B_4C and graphite particles adhering to different parts of the uncleaned FeB surface.

Furthermore, it is worth noting (contrary to what was claimed by Passerone *et al.*[43]) that FeB is wetted somewhat better by liquid Sn (around 10 to 30 deg, Table III) compared to the wettability of the steels below the borided surface, as according to Varanasi *et al.*,[71] the contact angle of liquid tin on nonoxidized steel surfaces varies between 20 and 40 deg. This is because the interaction of Fe and Sn leads to the formation of $FeSn_2$ (previously discussed), which is an intermetallic of not fully metallic bonds,[71] and so the adhesion energy at the $Sn/FeSn_2$ interface is lower compared to the Sn/FeB interface. This, combined with the same surface tension of the same liquid tin, leads to better wettability of FeB by liquid tin compared to weaker wettability of bare steel by the same liquid tin.

V. CONCLUSIONS

In this article, the applicability of the diffusion boriding process was studied to increase the lifetime of a wettable selective soldering tool. The following conclusions can be drawn from the tests performed.

1. Approximately 27- to 39-μm-thick coherent (FeB + Fe_2B) iron boride layer was formed on the surface, below which the layer had a sawtooth morphology. This coherent part of the layer prevents the contact between the solder melt and the base material.
2. After 40 days of continuous immersion testing of the borided samples in SAC309 solder melt, no reduction of thickness and no change in the morphology of the borided layer were observed for all examined steel substrates. Furthermore, no reaction phases formed at the FeB/SAC309 and Fe_2B/SAC309 interfaces and no element dissolution was detected between the borides and solder melt. Thus, it was shown that both FeB and Fe_2B phases are resistant against the aggressive SAC309 solder melt.
3. Thermodynamic calculations confirm the good corrosion resistance of the FeB and Fe_2B phases of the boride coatings toward liquid tin.
4. With the applied parameters, the SAC309 solder melt wets well the borided steels. The best values of the contact angle were measured for DC04 steel.
5. Subsequent oxidation of borided samples results in better wetting because the poorly wetted B_4C and graphite particles are removed from the surface by the oxidation treatment.

From this study, it can be stated that diffusion boriding is a suitable method to increase the lifetime of wettable selective soldering tools.

ACKNOWLEDGMENTS

The authors thank András Bartók for his assistance in the boriding process, Árpád Kovács for the SEM investigation, Zoltán Márkus for the sampling process, and Zoltánné Márkus for the sample preparation. The research was supported by the GINOP-2.3.2-15-2016-00027 project. The realization of this project is supported by the European Union and co-financed by the European Social Fund.

CONFLICT OF INTEREST

On behalf of all the authors, the corresponding author states that there is no conflict of interest.

FUNDING

Open access funding provided by University of Miskolc.

OPEN ACCESS

REFERENCES

1. H. Nishikawa, T. Takemoto, K. Kifune, T. Uetani, and N. Sekimori: *Mater. Trans.*, 2004, vol. 45, pp. 741–46. https://doi.org/10.2320/matertrans.45.741.

2. *Soldering Tips & Lifetime Issues "Coping with Lead Free,"* Cooper Industries, Ltd., Houston, TX, 2007. https://www.elexp.com/media/wysiwyg/cms-pdfs/Weller_Coping_with_Lead_Free.pdf, accessed 16 Aug 2021.
3. T. Takemoto, T. Uetani, and M. Yamazaki: *Sold. Surf. Mount. Technol.*, 2004, vol. 16, pp. 9–15. https://doi.org/10.1108/09540910410562473.
4. Y.W. Yen, B.J. Chen, and Y.S. Li: *8th Int. Microsystems, Packaging, Assembly and Circuits Technology Conf.*, 2013, p. 260..
5. T. Ishida: *Trans. JIM.*, 1973, vol. 14, pp. 37–44. https://doi.org/10.2320/matertrans1960.14.37.
6. A.N. Campbell, J.H. Wood, and G.B. Skinner: *J. Am. Chem. Soc.*, 1949, vol. 71, pp. 1729–33. https://doi.org/10.1021/ja01173a052.
7. Y.C. Huang, S.W. Chena, W. Gierlotka, C.H. Chang, and J.C. Wu: *J. Mater. Res.*, 2007, vol. 22, pp. 2924–29. https://doi.org/10.1557/JMR.2007.0361.
8. B.C. Scott and M.E. Warwick: *Trans. IMF.*, 1983, vol. 61, pp. 43–45. https://doi.org/10.1080/00202967.1983.11870635.
9. N. Tang, Y.P. Li, S. Kurosu, Y. Koizumi, H. Matsumoto, and A. Chiba: *Corr. Sci.*, 2012, vol. 60, pp. 32–37. https://doi.org/10.1016/j.corsci.2012.04.015.
10. N. Tang, Y. Li, Y. Koizumi, S. Kurosu, and A. Chiba: *Corr. Sci.*, 2013, vol. 75, pp. 262–68. https://doi.org/10.1016/j.corsci.2013.06.009.
11. G. Chen, L. Xue, J. Wang, Z. Tang, X. Li, and H. Dong: *Corr. Sci.*, 2020, vol. 174, pp. 1–11. https://doi.org/10.1016/j.corsci.2020.108836.
12. G. Chen, J. Wang, D. Wang, L. Xue, B. Zeng, B. Qin, and Z. Tang: *Corr. Sci.*, 2021, vol. 178, pp. 1–12. https://doi.org/10.1016/j.corsci.2020.109088.
13. F. Stromberg, W. Keune, V.E. Kuncser, and K. Westerholt: *Phys. Rev. B.*, 2005, vol. 72, pp. 1–11. https://doi.org/10.1103/PhysRevB.72.064440.
14. W.H. Tao, C. Chen, C.E. Ho, W.T. Chen, and C.R. Kao: *Chem. Mater.*, 2001, vol. 13, pp. 1051–56. https://doi.org/10.1021/cm000803l.
15. H. Nishikawa, A. Komatsu, and T. Takemoto: *Mater. Trans.*, 2005, vol. 46, pp. 2394–99. https://doi.org/10.2320/matertrans.46.2394.
16. J. Watanabe, N. Sekimori, K. Hatsuzawa, T. Uetani, and I. Shohji: *J. Phys. Conf. Ser.*, 2012, vol. 379, pp. 1–10. https://doi.org/10.1088/1742-6596/379/1/012025.
17. M. Benke, Z. Salyi, V. Takats, A. Csik, P. Rugoczky, and G. Kaptay: *Mater. Sci. Technol.*, 2019, vol. 35, pp. 680–86. https://doi.org/10.1080/02670836.2019.1582192.
18. M. Benke, Z. Salyi, and G. Kaptay: *J. Min. Metall. Sect. B-Metall.*, 2018, vol. 54, pp. 283–90. https://doi.org/10.2298/JMMB170918019B.
19. A.A. Joshi and S.S. Hosmani: *Mater. Manuf. Proc.*, 2014, vol. 29, pp. 1062–72. https://doi.org/10.1080/10426914.2014.921705.
20. A.J. Ninham and I.M. Hutchings: *J. Vac. Sci. Technol. A.*, 1986, vol. 4, pp. 2827–31. https://doi.org/10.1116/1.573686.
21. C.K.N. Oliveira, L.C. Casteletti, A.L. Neto, G.E. Totten, and S.C. Heck: *Vacuum.*, 2010, vol. 84, pp. 792–96. https://doi.org/10.1016/j.vacuum.2009.10.038.
22. M. Kulka, N. Makuch, A. Pertek, and A. Piasecki: *Mater. Charact.*, 2012, vol. 72, pp. 59–67. https://doi.org/10.1016/j.matchar.2012.07.009.
23. I. Uslu, H. Comert, M. Ipek, O. Ozdemir, and C. Bindal: *Mater. Des.*, 2007, vol. 28, pp. 55–61. https://doi.org/10.1016/j.matdes.2005.06.013.
24. L.X. Cai, J.R. Mao, S.S. Wang, J. Di, and Z.P. Feng: *J. Eng. Trib.*, 2015, vol. 229, pp. 636–45. https://doi.org/10.1177/1350650114557105.
25. A. Agarwal and N.B. Dahotre: *Metall. Mater. Trans. A.*, 2000, vol. 31A, pp. 401–408. https://doi.org/10.1007/s11661-000-0277-x.
26. B. Selcuka, R. Ipek, M.B. Karamis, and V. Kuzucu: *J. Mater. Proc. Technol.*, 2000, vol. 103, pp. 310–17. https://doi.org/10.1016/S0924-0136(99)00488-4.
27. C. Bindal and A. Erdemir: *Appl. Phys. Lett.*, 1996, vol. 68, pp. 923–25. https://doi.org/10.1063/1.116232.
28. M.A. Béjar and R. Henríquez: *Mater. Des.*, 2009, vol. 30, pp. 1726–28. https://doi.org/10.1016/j.matdes.2008.07.006.
29. M. Kulka, N. Makuch, and A. Piasecki: *Surf. Coat. Technol.*, 2017, vol. 325, pp. 515–32. https://doi.org/10.1016/j.surfcoat.2017.07.020.
30. M. Tabura, M. Izciler, F. Gulb, and I. Karacanc: *Wear.*, 2009, vol. 266, pp. 1106–12. https://doi.org/10.1016/j.wear.2009.03.006.
31. G. Liu, J. Xing, S. Ma, Y. Wang, and W. Guan: *J. Mater. Res.*, 2017, vol. 32, pp. 2381–88. https://doi.org/10.1557/jmr.2017.143.
32. W. Hodge, R.M. Evans, and A.F. Haskins: *J. Met.*, 1955, vol. 7, pp. 824–32. https://doi.org/10.1007/BF03377576.
33. R.H. Biddulph: *Thin Solid Films.*, 1977, vol. 45, pp. 341–47. https://doi.org/10.1016/0040-6090(77)90267-X.
34. Y. Wang, J. Xing, S. Ma, B. Zheng, G. Liu, D. Yang, and Y. Bai: *Corr. Sci.*, 2016, vol. 104, pp. 260–68. https://doi.org/10.1016/j.corsci.2015.12.018.
35. D.N. Tsipas, G.K. Triantafyllidis, J. Kipkemoi Kiplagat, and P. Psillaki: *Mater. Lett.*, 1998, vol. 37, pp. 128–31. https://doi.org/10.1016/S0167-577X(98)00077-9.
36. D.C. Lou, O.M. Akselsen, M.I. Onsøien, J.K. Solberg, and J. Berget: *Surf. Coat. Technol.*, 2006, vol. 200, pp. 5282–88. https://doi.org/10.1016/j.surfcoat.2005.06.026.
37. H.P. Yang, X.C. Wu, Y.A. Min, T.R. Wu, and J.Z. Gui: *Surf. Coat. Technol.*, 2013, vol. 228, pp. 229–33. https://doi.org/10.1016/j.surfcoat.2013.04.033.
38. D.K. Popowska, A.P. Owsianna, A. Bartkowska, D. Bartkowski, and D. Przestacki: *J. Res. Appl. Agr. Eng.*, 2014, vol. 59, pp. 40–45.
39. G. Kartal, O. Kahvecioglu, and S. Timur: *Surf. Coat. Technol.*, 2006, vol. 200, pp. 3590–93. https://doi.org/10.1016/j.surfcoat.2005.02.210.
40. G.K. Kariofillis, G.E. Kiourtsidis, and D.N. Tsipas: *Surf. Coat. Technol.*, 2005, vol. 201, pp. 19–24. https://doi.org/10.1016/j.surfcoat.2005.10.025.
41. G. Liu, J. Xing, S. Ma, Y. He, H. Fu, Y. Gao, Y. Wang, and Y. Wang: *Metall. Mater. Trans. A.*, 2015, vol. 46A, pp. 1900–907. https://doi.org/10.1007/s11661-015-2820-9.
42. S. Ma, Z. Huang, J. Xing, G. Liu, Y. He, H. Fu, Y. Wang, Y. Li, and D. Yi: *J. Mater. Res.*, 2015, vol. 30, pp. 257–65. https://doi.org/10.1557/jmr.2014.383.
43. A. Passerone, M.L. Muolo, and D. Passerone: *J. Mater. Sci.*, 2006, vol. 41, pp. 5088–98. https://doi.org/10.1007/s10853-006-0442-8.
44. P. Baumli, J. Sytchev, and G. Kaptay: *J. Mater. Sci.*, 2010, vol. 45, pp. 5177–90. https://doi.org/10.1007/s10853-010-4555-8.
45. S.V. Devyatkin and G. Kaptay: *J. Solid. State Chem.*, 2000, vol. 154, pp. 107–9. https://doi.org/10.1006/jssc.2000.8819.
46. European Steel and Alloy Grades/Numbers, SteelNumber database: http://www.steelnumber.com/en/steel_composition_eu.php?name_id=201, accessed 16 Aug 2021.
47. European Steel and Alloy Grades/Numbers, SteelNumber database: http://www.steelnumber.com/en/steel_composition_eu.php?name_id=152, accessed 16 Aug 2021.
48. European Steel and Alloy Grades/Numbers, SteelNumber database: http://www.steelnumber.com/en/steel_composition_eu.php?name_id=190, accessed 16 Aug 2021.
49. European Steel and Alloy Grades/Numbers, SteelNumber database: http://www.steelnumber.com/en/steel_composition_eu.php?name_id=969, accessed 16 Aug 2021.
50. A. Molnar, M. Benke, and Z. Gacsi: *Arch. Metall. Mater.*, 2017, vol. 62, pp. 1063–66. https://doi.org/10.1515/amm-2017-0154.
51. Safety Data Sheet: http://alu-forr.hu/images/INOfluX_HU.pdf.
52. L. Somlyai-Sipos and P. Baumli: *Res. Discov.*, 2017, vol. 2, pp. 9–12. https://doi.org/10.1556/2051.2017.00039.
53. M. Czagány, D. Varanasi, A. Sycheva, D. Janovszky, D. Koncz-Horváth, F. Kristaly, P. Baumli, and G. Kaptay: *J. Mater. Sci.*, 2020, vol. 56, pp. 7823–39. https://doi.org/10.1007/s10853-020-05522-5.
54. I. Barin: *Thermochemical Properties of Pure Substances*, Wiley-VCH, Weinheim, 1993, in 2 parts.
55. X. Wang, B. Zhou, Z. Guo, Y. Liu, J. Wang, and X. Su: *Calphad.*, 2017, vol. 57, pp. 88–97. https://doi.org/10.1016/j.calphad.2017.03.006.

56. T.B. Massalski: *Binary Alloy Phase Diagrams*, 2nd ed., ASM International, Materials Park, OH, 1990, vol. 3, p. 3589. https://doi.org/10.1002/adma.19910031215.
57. J. Emsley: *The Elements*, Clarendon Press, Oxford, UK, 1989https://doi.org/10.1002/ange.19901020140,ISBN0-19-855237-8.
58. Y. Ohishi, M. Sugizaki, Y. Sun, H. Muta, and K. Kurosaki: *J. Nucl. Sci. Technol.*, 2019, vol. 56, pp. 859–65. https://doi.org/10.1080/00223131.2019.1593893.a.
59. F. Nakamani, Y. Ohishi, M. Kumagai, H. Muta, K. Kurosaki, K.I. Fukumoto, and S. Yamanak: *Nippon Genshiryoku.*, 2016, vol. 15, pp. 223–28. https://doi.org/10.3327/taesj.J16.005.
60. G. Kaptay: *Adv. Coll. Inter. Sci.*, 2018, vol. 256, pp. 163–92. https://doi.org/10.1016/j.cis.2018.04.007.
61. N. Suwattananont, Ć Roumiana, and S. Petrova: *Oxid. Met.*, 2008, vol. 70, pp. 307–15. https://doi.org/10.1007/s11085-008-9123-0.
62. J. Ptačinová, M. Drienovský, M. Palcut, R. Čička, M. Kusý, and M. Hudáková: *Kovove Mater.*, 2015, vol. 53, pp. 1–12. https://doi.org/10.4149/km-2015-3-175.
63. E. Dokumaci, I. Özkan, and B. Önay: *Surf. Coat. Technol.*, 2013, vol. 232, pp. 22–25. https://doi.org/10.1016/j.surfcoat.2013.04.047.
64. K. Li, Z. Huang, S. Wang, Y. Shen, W. Wang, and Y. Jian: *Mater. Res. Exp.*, 2019, vol. 6(10), pp. 1–10. https://doi.org/10.1088/2053-1591/ab35a3.
65. G. Kaptay, E. Báder, and L. Bolyán: *Mater. Sci. Forum.*, 2000, vol. 329–330, pp. 151–56. https://doi.org/10.4028/www.scientific.net/MSF.329-330.151.
66. Z. Weltsch, A. Lovas, J. Takács, Á. Cziráki, A. Tóth, and G. Kaptay: *Appl. Surf. Sci.*, 2013, vol. 268, pp. 52–60. https://doi.org/10.1016/j.apsusc.2012.11.150.
67. R. Asthana: *Metall. Mater. Trans. A.*, 1994, vol. 25A, pp. 225–30. https://doi.org/10.1007/BF02646692.
68. N. Froumin, N. Frage, M. Aizenshtein, and M.P. Dariel: *J. Eur. Ceram. Soc.*, 2003, vol. 23, pp. 2821–28. https://doi.org/10.1016/S0955-2219(03)00294-2.
69. S.A. Sánchez, J. Narciso, E. Louis, F. Rodríguez-Reinoso, E. Saiz, and A. Tomsia: *Mater. Sci. Eng. A.*, 2008, vol. 495, pp. 187–91. https://doi.org/10.1016/j.msea.2007.09.090.
70. N. Eustathopoulos: *Metals.*, 2015, vol. 5, pp. 350–70. https://doi.org/10.3390/met5010350.
71. D. Varanasi, K.E. Aldawoudi, P. Baumli, D. Koncz-Horvath, and G. Kaptay: *Arch. Metall. Mater.*, 2021, vol. 66, pp. 469–76. https://doi.org/10.24425/amm.2021.135880.